NJC

PAPER

View Article Online
View Journal | View Issue

Cite this: *New J. Chem.*, 2019, **43**, 9274

A mechanism of the luminescent covalent organic framework for the detection of NH_3†

Yanan Yang, Zhengyan Zhao, Yang Yan, Guanglan Li and Ce Hao *

Received 15th January 2019,
Accepted 15th May 2019

DOI: 10.1039/c9nj00243j

rsc.li/njc

The interaction between a luminescent covalent organic framework (COF) and the indoor pollutant NH_3 was investigated based on density functional theory and time-dependent density functional theory. The frontier molecular orbitals and electronic configuration showed that the luminescence mechanism of the COF was strongly affected by the hydrogen bond between the COF and NH_3. In addition, the calculated hydrogen bond length, infrared (IR) spectra, and proton nuclear magnetic resonance (^{1}H NMR) spectroscopy analysis indicated that the hydrogen bond in the S_1 state was enhanced, which is identical to the calculated results of electronic excitation energies. The fluorescence rate coefficient of the COF was reduced when interacting with NH_3. The hydrogen bond between the COF and NH_3 in the S_1 state is critical for the COF luminescence properties, which means that the COF shows potential application in the detection of NH_3.

Introduction

As a major indoor pollutant, NH_3 is extremely harmful to human health. Prolonged exposure to high concentrations of NH_3 will burn the eyes, skin, throat and lungs. Also, inhaling even low concentrations of NH_3 can cause cough, headache, fever, nausea and vomiting.[1–5] The conventional methods for detecting NH_3 include spectrophotometry, ion chromatography and gas-sensitive electrode.[1,6,7] However, the emergence of optical chemical sensors has created new opportunities for indoor pollutant detection. The optical chemical sensor, which detects the substance by the fluorescence change arising from the interaction between the detected substance and the sensitive layer, has good selectivity, high sensitivity and convenience of use.[1,8–12] Covalent organic frameworks (COFs) are an emerging class of porous crystal materials whose building blocks are connected by strong covalent bonds and are composed of low molecular weight elements.[13–15] They exhibit great advantages over other materials, including low density, high luminescence intensity, large porosity, good thermal stability and multiple binding sites; thus, they have aroused widespread interest in recent years.[16–22] The application of COFs as fluorescent chemical sensors has been reported.[23–26] For instance, in 2016, Dalapati *et al.*[27] used the photoluminescent two-dimensional (2D) COF (TPE-Ph COF) as a sensor to detect NH_3 with high sensitivity. Recently, Gao *et al.*[28] synthesized a highly luminescent 2D COF (Py-TPE-COF) that can detect 2,4,6-trinitrophenol up to the ppm level.

Numerous studies have shown that hydrogen bonding has, to a large extent, a major influence on the luminescence system.[29–31] Based on "the excited-state hydrogen-bonding dynamics",[32] when the hydrogen-bonded complex is photoexcited, the charge in every electronic state reorganizes. Then, the structure of the compound readjusts, and hydrogen bonding interactions also undergo the corresponding dynamic changes. Although various femtosecond time-resolved spectroscopy techniques are currently applied to monitor the excited-state hydrogen-bonding behavior,[30,33,34] ultrafast spectroscopy still cannot be used alone due to the limitation of spectral resolution of femtosecond laser pulses.[33] After years of development, the time-dependent density functional theory (TDDFT) approach effectively solves the problem of excited-state hydrogen-bonding dynamics and has been successfully applied to study the excited states of various complex molecular systems.[29,32,35]

Huang *et al.*[36] synthesized a photoresponsive 2D COF (Ph-An-COF) with a pore diameter of 2.9 nm by condensation of 1,3,5-benzenetriboronic acid and 2,3,6,7-tetrahydroanthracene under solvothermal conditions. Ph-An-COF shows a maximum emission peak at 429 nm and emits strong blue fluorescence. In this work, the hydrogen bond interaction between Ph-An-COF and NH_3 was investigated by density functional theory (DFT) and TDDFT methods. The analysis of the frontier molecular orbitals (MOs) and electronic configuration shows the change of the luminescence mechanism before and after hydrogen bonding interaction. The hydrogen-bonding dynamics in the S_1 state were studied by comparing the hydrogen bond lengths, infrared (IR) spectra and proton nuclear magnetic resonance (^{1}H NMR) of the S_0 and S_1 states.

State Key Laboratory of Fine Chemicals, School of Petroleum and Chemical Engineering, Dalian University of Technology, Panjin campus, 124221, China. E-mail: haoce@dlut.edu.cn; Fax: +86-411-84986335; Tel: +86-411-84986335

† Electronic supplementary information (ESI) available. See DOI: 10.1039/c9nj00243j

In addition, we also examined the influence of the excited-state hydrogen bond on Ph-An-COF fluorescence rate constants and the feasibility of detecting NH_3 by Ph-An-COF.

Computational methods

Geometry optimizations, UV-vis spectrum, IR spectra and ^{1}H NMR were analyzed by DFT and TDDFT methods with B3LYP-D3 (BJ), the dispersion-corrected B3LYP functional with Beck-Johnson damping, of the Gaussian 09 software.[37,38] The 6-311G(d,p) basis set was selected for geometric optimization, since it can properly describe the molecular structure. Frequency calculations were performed at the same theoretical level to confirm that the optimized geometric structures were at stable points without imaginary frequency. However, for UV-vis spectrum and ^{1}H NMR, the 6-311G(d,p) basis set cannot meet the accuracy requirements, so we selected the higher 6-311++G(d,p) basis set to calculate the UV-vis spectrum and ^{1}H NMR.[39–41] The IR spectra were corrected using a correction factor of 0.967.[42]

We calculated the electronic configuration with the TZP basis set and B3LYP hybrid functional in the ADF 2012 software.[43]

The fluorescence rate coefficients were calculated based on the frequency results computed by Gaussian software and employing the MOMAP software package.[44,45]

Results and discussion

Computational model

As shown in Fig. 1(a), Ph-An-COF is a hexagonal porous crystal material with periodic structure. The first principles method fails to provide an effective way to calculate the excited state with periodic systems. Therefore, we selected a representative structural fragment from the periodic Ph-An-COF for the subsequent study. The optimized geometric configuration of the truncated structural fragment is shown in Fig. 1(b), which is referred to as complex **1**.

We computed the geometric parameters, UV-vis maximum absorption peak and vibration frequencies for the structural fragment, as listed in Table 1, and compared them with the corresponding experimental values. The calculated values of bond lengths and bond angles, together with the vibration frequencies, are well matched with the experimental values. Furthermore, the calculated maximum UV-vis absorption peak at 280 nm is almost the same as the experimental value of 278 nm. Therefore, it can be deduced from the aspects of geometric structure, electronic structure and vibration frequencies that the truncated structural unit of Ph-An-COF is credible and can represent the whole Ph-An-COF.

Table 1 The experimental and calculated results of geometry, vibration frequencies and electronic structure of complex **1**

	Exp. values[36]	Calc. values
Bond lengths/Å		
C45–C10	1.41	1.40
B9–C10	1.55	1.54
B9–O17	1.40	1.39
O17–C18	1.38	1.38
C18–C19	1.36	1.36
Bond angles/deg.		
C45–C10–B9	121.4	120.8
C10–B9–O17	124.7	124.5
B9–O17–C18	106.6	106.0
O17–C18–C19	129.3	129.0
Vibration frequencies/cm^{-1}		
ν(benzene C=C)	1594	1592
ν(anthracene C=C)	1456	1463
ν(B–O)	1308	1301
ν(C–O)	1206	1211
UV-vis maximum absorption/nm	278	280

In order to investigate the hydrogen bond dynamics between Ph-An-COF and NH_3, one NH_3 molecule and complex **1** were used to form various hydrogen-bonded complexes. The periodic structure of Ph-An-COF (Fig. 1a) reveals 3 equivalent sites (1, 2 and 3) for the hydrogen bonding. Three corresponding hydrogen-bonded complexes were optimized, and the one with the lowest energy was located at site 2. Position 2 has two hydrogen bonds, and the other two positions have only one hydrogen bond. We selected the

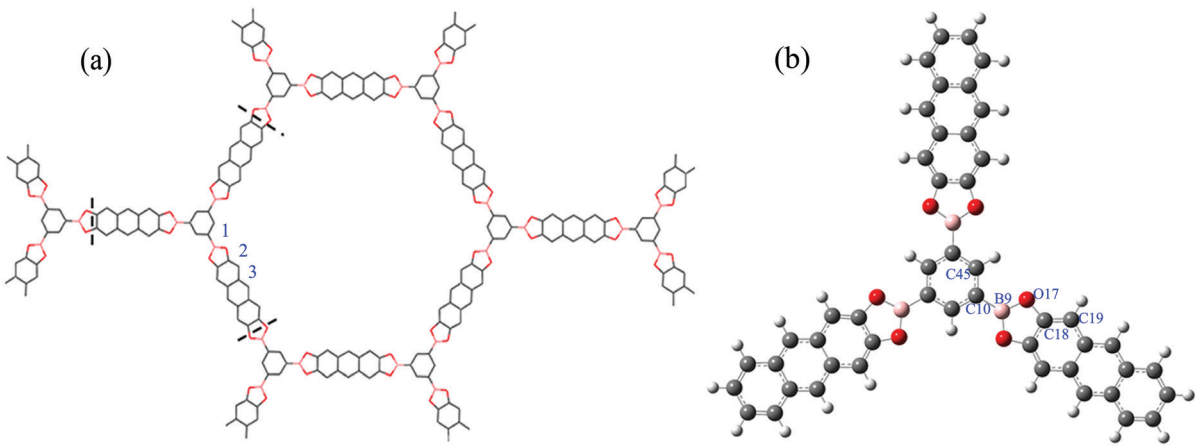

Fig. 1 (a) The crystal structure of Ph-An-COF, with dashed lines representing the truncation position for the fragment shown in (b); 1, 2 and 3 are binding sites for NH_3. (b) The optimized representative structural fragment (grey: C atom; pink: B atom; red: O atom; white: H atom).

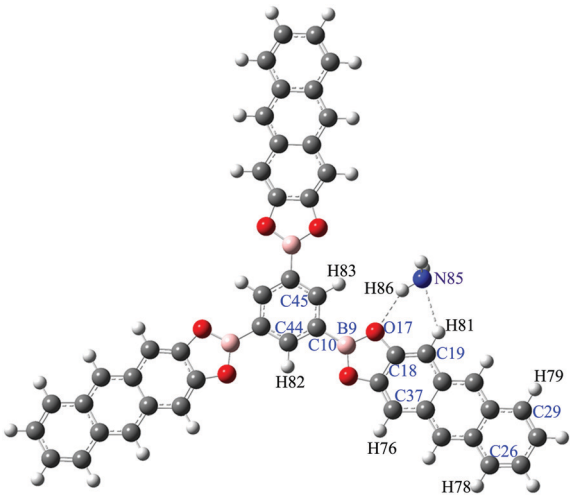

Fig. 2 The lowest-energy hydrogen-bonded complex formed by NH_3 and structural elements; the dashed lines represent hydrogen bonds (grey: C atom; pink: B atom; red: O atom; white: H atom; blue: N atom).

hydrogen-bonded complex with the lowest energy (Fig. 2) for further study, which was designated as complex **2**.

Frontier molecular orbitals (MOs) and electronic configuration

The frontier MOs and electronic configuration can clearly explain the luminescence mechanism. Kasha[46] proposed that the fluorescence quantum yield can only be detected when the electrons transit from the lowest excited singlet state to the ground state. Thus, we just need to examine the S_1 and S_0 states related to luminescence, which mainly correspond to the transition of electrons from the lowest unoccupied molecular orbital (LUMO) to the highest occupied molecular orbital (HOMO).

As shown in Fig. 3, the LUMO electron density for complex **1** is mainly distributed on the 1,3,5-benzenetriboronic acid ligand and on all 2,3,6,7-tetrahydroxyanthracene ligands, whereas the HOMO electron density is entirely distributed on the 2,3,6,7-tetrahydroxyanthracene ligands. However, the LUMO electron density of complex **2** is mainly distributed on the 1,3,5-benzenetriboronic acid ligand and the 2,3,6,7-tetrahydroxyanthracene ligands far away from the NH_3 molecule, while the HOMO electron density is distributed on the 2,3,6,7-tetrahydroxyanthracene ligand near the NH_3 molecule. Thus, we believe that the hydrogen bonds between Ph-An-COF and NH_3 affect the luminescence behavior of Ph-An-COF by changing the distribution of the electron density.

To further determine whether hydrogen bonding alters the luminescence mechanism of Ph-An-COF, we analyzed the electronic configurations of both structures. The results of the analysis shown in Fig. 3 reveal that the LUMOs of both structures are mainly made up of π^* orbitals of B atoms and C atoms, while the HOMOs are mostly made up of π orbitals of O atoms and C atoms. It is noticeable that the contribution of the atomic orbital is different even though both structures have the same orbital composition. The contributions of B and C atoms to the LUMO for complex **1** are 9.54% and 87.60%, respectively, while those of B and C atoms for complex **2** are 9.61% and 86.06%, respectively. Additionally, the contributions of C and O atoms to

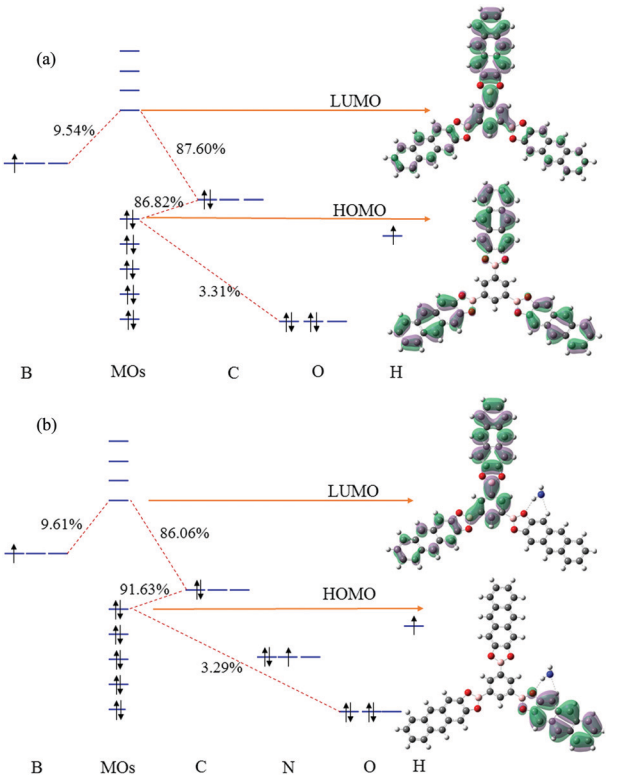

Fig. 3 The frontier molecular orbitals and electronic configurations of (a) complex **1** and (b) complex **2** (green: positive sign; purple: negative sign).

HOMO for complex **1** are 86.82% and 3.31%, respectively, while those of C and O atoms for complex **2** are 91.63% and 3.29%, respectively. Thus, the above analysis leads to the conclusion that the hydrogen bonds between Ph-An-COF and NH_3 alter the luminescence mechanism by changing the composition of the LUMO and HOMO.

The calculated electronic excitation energies

As previously reported, hydrogen bonding markedly affects the electronic excitation process. After photoexcitation, the excitation energies will clearly change due to the redistribution of the charge of each electronic state in complex **2**, which makes the charge contribution for complex **2** significantly different from that for complex **1**.[47] According to an earlier report, the existence of hydrogen bonding would cause a change in the energy gap, resulting in the shift of the electronic spectrum. In other words, if the energy gap decreases (strengthening of the excited-state hydrogen bonding), the electronic spectrum will be red-shifted. In contrast, if the energy gap increases (weakening of the excited-state hydrogen bonding), the electronic spectrum will be blue-shifted.[32] As listed in Table 2, we computed the respective excitation energies of the structural unit and the most stable hydrogen-bonded complex with the TDDFT method on the basis of the optimization. We mostly paid attention to the S_1 state due to Kasha's rule. We found that the first excitation energy of the hydrogen-bonded complex (complex **2**) was decreased by 0.07 eV compared with the structural unit (complex **1**), which indicated

Table 2 Electronic excitation energy of complex **1** and complex **2**

Excited states	Complex **1** (eV)	Complex **2** (eV)
S_1	3.10	3.03
S_2	3.10	3.04
S_3	3.10	3.09
S_4	3.18	3.10
S_5	3.18	3.17
S_6	3.18	3.22
S_7	3.31	3.22

that the electronic spectrum is red-shifted. Thus, we assume that the hydrogen bonding is enhanced in the S_1 state.

Hydrogen bonding behavior in the S_1 state

To gain deeper understanding of the hydrogen bonding in the S_1 state, we analyzed the hydrogen bond properties of complex **2** in this state from three aspects, namely, the geometric configuration, ^{1}H NMR of related H atom, and IR spectra.

The TDDFT method was used to optimize the S_1 state geometric configuration for complex **2**. The results, listed in Table 3, reveal that the bond length of H86–N85···H81–C19 varies from 2.51 Å (S_0) to 2.29 Å (S_1), a decrease of about 0.22 Å. However, the bond length of N85–H86···O17–B9 varies from 2.19 Å (S_0) to 2.29 Å (S_1), an increase of 0.1 Å. Since the hydrogen bond length change of N85–H86···O17–B9 is very small and within the margin of error (0.1 Å), the hydrogen bond H86–N85···H81–C19 plays a more important role compared with N85–H86···O17–B9, considering the calculated results of the electronic excitation energies.

The ^{1}H NMR chemical shift can be used to measure the change of hydrogen bond strength.[32,48] We mainly focused on the ^{1}H NMR chemical shift of H81. The results presented in Table 3 reveal that ^{1}H NMR results of H81 in the S_0 and S_1 states are 22.18 ppm and 21.30 ppm, respectively. The chemical shift of the hydrogen atom that forms the hydrogen bond shifts upfield, and the H atom nucleus density increases, indicating that the hydrogen bond H86–N85···H81–C19 in the S_1 state becomes stronger.

We can gain insight into the hydrogen bonding behavior in the S_1 state by evaluating the vibrational frequencies of the characteristic groups in which the hydrogen bond is located.[33,49] As shown in Fig. 4, we adopted DFT and TDDFT approaches to calculate the IR spectra for complex **2** in the S_0 and S_1 states, respectively, and compared the stretching vibration frequencies of the groups forming hydrogen bonds. The data clearly show that vibration frequencies of C19–H81 and N85–H86 in the S_0 state are

Table 3 Hydrogen bond length of complex **2** and chemical shift of ^{1}H NMR of H81 atom in the S_0 and S_1 states

	S_0	S_1
Bond lengths/Å		
H86–N85···H81–C19	2.51	2.29
N85–H86···O17–B9	2.19	2.29
^{1}H NMR/ppm		
H81	22.18	21.30

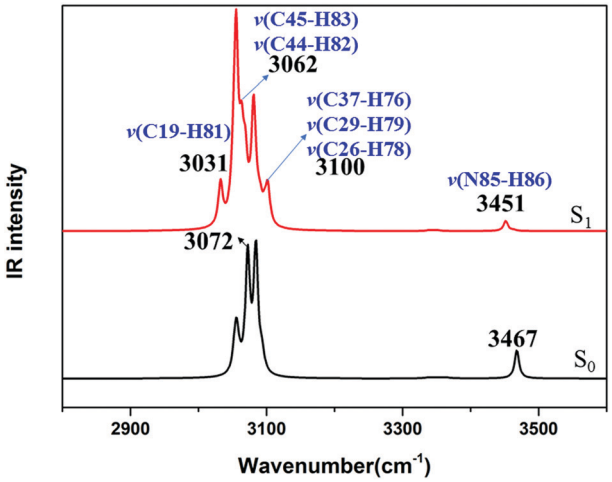

Fig. 4 Schematic diagram of the vibration frequencies of complex **2** in the S_0 and S_1 states.

3072 cm^{-1} and 3467 cm^{-1}, respectively, while in the S_1 state, their vibration frequencies are 3031 cm^{-1} and 3451 cm^{-1}, respectively. The enhancement of hydrogen bonds in the excited state can weaken the stretching vibration frequencies of the groups that form the hydrogen bond, thus leading to the red-shift of infrared spectra. The red-shift for these characteristic stretching bands demonstrates that the hydrogen bond H86–N85···H81–C19 is increased in the S_1 state.[32,33] In addition, two new peaks appear in the S_1 state due to the combination of the vibration intensities of several groups. The stretching vibration frequencies of C45–H83 and C44–H82 are located at 3062 cm^{-1}, and the stretching vibration frequencies of C37–H76, C29–H79 and C26–H78 are located at 3100 cm^{-1}.

To sum up, the findings on the hydrogen bond lengths and the vibrational frequencies of characteristic groups, together with the ^{1}H NMR chemical shift of the related H atom for complex **2**, clearly demonstrate that hydrogen bonding is enhanced in the S_1 state, which is in agreement with the previous prediction of the electronic transition energies.

The influence of hydrogen bonding on luminescence

The relationship between the enhancement of the excited-state hydrogen bonding and luminescence is illustrated in Fig. S1 (ESI†). We can see that the energy gap of the no-hydrogen-bond system is larger than that of the hydrogen-bond system ($\Delta E_{\text{no-HB}} > \Delta E_{\text{HB}}$). This is due to enhancement of the excited-state hydrogen bond, which leads to a smaller downshift of the S_0 state energy level compared with its S_1 state ($\Delta E_{\text{GS}} < \Delta E_{\text{ES}}$). According to the energy gap rule, the stronger hydrogen bonding enhances the nonradiative transition rate. Since nonradiative transition competes with radiative transition, the rate of radiative transition will decrease.[32,50] Consequently, the enhancement of excited-state hydrogen bond may weaken the fluorescence intensity of Ph-An-COF.

The rate constant of various deactivation processes can be predicted by using Fermi's golden rule and time-dependent perturbation theory. The relation between rate coefficient and

Table 4 The fluorescence rate coefficients of complex **1** and complex **2**

	Complex **1**	Complex **2**
Fluorescent rate constants k_F/s^{-1}	1.78×10^6	7.97×10^5

the perturbation matrix element from Fermi's golden rule is as follows:

$$k_{if} = \frac{2\pi}{\hbar}\sum_{v,v'} P_{i,v}\left|H_{iv,fv'}{}'\right|^2 \delta(E_{f,v'} - E_{i,v}),$$

where v and i are the initial vibrational state and electronic state, respectively; v′ and f are the vibrational state and electronic state after the transition, respectively; $E_{i,v}$ is the initial state energy; $E_{f,v'}$ is the final state energy; δ is the Dirac function; and $P_{i,v}$ is the Boltzmann distribution coefficient.[51]

Based on Fermi's golden rule, the fluorescence emission rate coefficient k_F can be expressed as:

$$k_F = \int \frac{4\omega}{3\hbar c^3}\sum_{v,v'} P_{i,v}\left|\langle\psi_{i,v}|\mu|\psi_{f,v'}\rangle\right|^2 \delta(\omega_{i,v} - \omega)\mathrm{d}\omega,$$

where ω denotes the circular frequency; $\psi_{i,v}$ and $\psi_{f,v'}$ are the wave functions of the initial and final states, respectively; μ denotes the electronic transition dipole moment between the two states; and c represents the speed of light in vacuum.[44]

The fluorescence rate coefficients for both structures are 1.78×10^6 s^{-1} (complex **1**) and 7.97×10^5 s^{-1} (complex **2**), as listed in Table 4. Clearly, the fluorescence rate coefficient of complex **1** is about two-fold that of complex **2**. Also, the fluorescence intensity is positively correlated with the fluorescence rate coefficient. In other words, the fluorescence intensity will be obviously reduced after fluorescent Ph-An-COF interacts with the indoor pollutant NH_3.

The recognition of small molecules by fluorescent materials can be achieved by detecting the changes in fluorescence intensity. Given that the fluorescence rate coefficient of Ph-An-COF decreased after interacting with NH_3, we believe that Ph-An-COF has potential application prospects in detecting the indoor pollutant NH_3.

Conclusions

In this work, we studied the effect of the intermolecular hydrogen bond formed between NH_3 and Ph-An-COF in the electronically excited state on the luminescence behavior of Ph-An-COF *via* DFT and TDDFT methods. The calculated values of the structural unit from the aspects of its geometric structure, vibration frequencies and UV-vis maximum absorption peak corresponded well with the experimental values, demonstrating that the structural unit could represent the periodic structure of Ph-An-COF. The analysis of the frontier molecular orbitals and electronic configuration indicated that the intermolecular hydrogen bonding in complex **2** altered the LUMO and HOMO compositions and thereby changed the mechanism of luminescence. The shortening of the hydrogen bond length, the red-shift of hydrogen bond donor–acceptor vibration modes, and the upfield shift of the hydrogen atom ^{1}H NMR band in the S_1 state revealed that the hydrogen bond was enhanced, consistent with the prediction of the excitation energy. In addition, the relationship between the luminescent properties and the excited-state hydrogen bond enhancement was evaluated, and the fluorescence rate coefficients were calculated. The fluorescence rate coefficient of Ph-An-COF decreased in the presence of NH_3, indicating that Ph-An-COF holds promise for fluorescence detection of the indoor pollutant NH_3. In addition, our study provides theoretical guidance for the detection of other small molecules.

Conflicts of interest

There are no conflicts to declare.

Acknowledgements

This work was supported by the National Science Foundation of China (Grant No. 21677029).

Notes and references

1 B. Timmer, W. Olthuis and A. V. D. Berg, *Sens. Actuators, B*, 2005, **107**, 666–677.
2 Y. Xiong, W. Xu, D. Ding, W. Lu, L. Zhu, Z. Zhu, Y. Wang and Q. Xue, *J. Hazard. Mater.*, 2018, **341**, 159–167.
3 L. S. K. Achary, A. Kumar, B. Barik, P. S. Nayak, N. Tripathy, J. P. Kar and P. Dash, *Sens. Actuators, B*, 2018, **272**, 100–109.
4 X. Li, X. Li, Z. Li, J. Wang and J. Zhang, *Sens. Actuators, B*, 2017, **240**, 273–277.
5 H. Fu, J. Zhang, J. Ding, Q. Wang, H. Li, M. Shao, Y. Liu, Q. Liu, M. Zhang, Y. Zhu and C. Yang, *Opt. Commun.*, 2018, **427**, 331–334.
6 K. Mistewicz, M. Nowak, D. Stróż and A. Guiseppi-Elie, *Talanta*, 2018, **189**, 225–232.
7 F. Valentini, V. Biagiotti, C. Lete, G. Palleschi and J. Wang, *Sens. Actuators, B*, 2007, **128**, 326–333.
8 B. Manna, A. K. Chaudhari, B. Joarder, A. Karmakar and S. K. Ghosh, *Angew. Chem., Int. Ed.*, 2013, **52**, 998–1002.
9 X. Wang, H. Zeng, L. Zhao and J. Lin, *Talanta*, 2006, **70**, 160–168.
10 G. Yang, J. Zhang, S. Zhu, Y. Wang, X. Feng, M. Yan and J. Yu, *Sens. Actuators, B*, 2018, **261**, 51–57.
11 H. Xie, J. Liang, Z. Zhang, Y. Liu, Z. He and D. Pang, *Spectrochim. Acta, Part A*, 2004, **60**, 2527–2530.
12 N. Xu, R. Wang, D. Li, Z. Zhou, T. Zhang, Y. Xie and Z. Su, *New J. Chem.*, 2018, **42**, 13367–13374.
13 X. Chen, M. Addicoat, S. Irle, A. Nagai and D. Jiang, *J. Am. Chem. Soc.*, 2012, **135**, 546–549.
14 L. A. Baldwin, J. W. Crowe, M. D. Shannon, C. P. Jaroniec and P. L. McGrier, *Chem. Mater.*, 2015, **27**, 6169–6172.
15 L. Ascherl, T. Sick, J. T. Margraf, S. H. Lapidus, M. Calik, C. Hettstedt, K. Karaghiosoff, M. Döblinger, T. Clark, K. W. Chapman, F. Auras and T. Bein, *Nat. Chem.*, 2016, **8**, 310–316.

16 A. Nagai, Z. Guo, X. Feng, S. Jin, X. Chen, X. Ding and D. Jiang, *Nat. Commun.*, 2011, **2**, 536.
17 H. Xu, J. Gao and D. Jiang, *Nat. Chem.*, 2015, **7**, 905–912.
18 S. Kandambeth, V. Venkatesh, D. B. Shinde, S. Kumari, A. Halder, S. Verma and R. Banerjee, *Nat. Commun.*, 2015, **6**, 6786.
19 E. Jin, J. Li, K. Geng, Q. Jiang, H. Xu, Q. Xu and D. Jiang, *Nat. Commun.*, 2018, **9**, 4143.
20 J. W. Crowe, L. A. Baldwin and P. L. McGrier, *J. Am. Chem. Soc.*, 2016, **138**, 10120–10123.
21 X. Han, Q. Xia, J. Huang, Y. Liu, C. Tan and Y. Cui, *J. Am. Chem. Soc.*, 2017, **139**, 8693–8697.
22 S. Dalapati, C. Gu and D. Jiang, *Small*, 2016, **12**, 6513–6527.
23 P. Das and S. K. Mandal, *J. Mater. Chem. A*, 2018, **6**, 16246–16256.
24 G. Das, B. P. Biswal, S. Kandambeth, V. Venkatesh, G. Kaur, M. Addicoat, T. Heine, S. Verma and R. Banerjee, *Chem. Sci.*, 2015, **6**, 3931–3939.
25 C. Zhang, S. Zhang, Y. Yan, F. Xia, A. Huang and Y. Xian, *ACS Appl. Mater. Interfaces*, 2017, **9**, 13415–13421.
26 T. Wang, R. Xue, H. Chen, P. Shi, X. Lei, Y. Wei, H. Guo and W. Yang, *New J. Chem.*, 2017, **41**, 14272–14278.
27 S. Dalapati, E. Jin, M. Addicoat, T. Heine and D. Jiang, *J. Am. Chem. Soc.*, 2016, **138**, 5797–5800.
28 Q. Gao, X. Li, G. Ning, K. Leng, B. Tian, C. Liu, W. Tang, H. Xu and K. P. Loh, *Chem. Commun.*, 2018, **54**, 2349–2352.
29 Y. Yao, X. Song, J. Qiu and C. Hao, *J. Phys. Chem. A*, 2014, **118**, 6191–6196.
30 G. Zhao, J. Liu, L. Zhou and K. Han, *J. Phys. Chem. B*, 2007, **111**, 8940–8945.
31 H. Xue, Y. Yan, Y. Hou, G. Li and C. Hao, *New J. Chem.*, 2018, **42**, 11485–11492.
32 G. Zhao and K. Han, *Acc. Chem. Res.*, 2012, **45**, 404–413.
33 G. Zhao and K. Han, *J. Phys. Chem. A*, 2007, **111**, 2469–2474.
34 G. Zhao and K. Han, *Biophys. J.*, 2008, **94**, 38–46.
35 C. Adamo and D. Jacquemin, *Chem. Soc. Rev.*, 2012, **42**, 845–856.
36 N. Huang, X. Ding, J. Kim, H. Ihee and D. Jiang, *Angew. Chem., Int. Ed.*, 2015, **54**, 8704–8707.
37 M. J. Frisch, G. W. Trucks, H. B. Schlegel, G. E. Scuseria, M. A. Robb, J. R. Cheeseman, G. Scalmani, V. Barone, B. Mennucci, G. A. Petersson, H. Nakatsuji, M. Caricato, X. Li, H. P. Hratchian, A. F. Izmaylov, J. Bloino, G. Zheng, J. L. Sonnenberg, M. Hada, M. Ehara, K. Toyota, R. Fukuda, J. Hasegawa, M. Ishida, T. Nakajima, Y. Honda, O. Kitao, H. Nakai, T. Vreven, J. A. Montgomery Jr, J. E. Peralta, F. Ogliaro, M. Bearpark, J. J. Heyd, E. Brothers, K. N. Kudin, V. N. Staroverov, R. Kobayashi, J. Normand, K. Raghavachari, A. Rendell, J. C. Burant, S. S. Iyengar, J. Tomasi, M. Cossi, N. Rega, J. M. Millam, M. Klene, J. E. Knox, J. B. Cross, V. Bakken, C. Adamo, J. Jaramillo, R. Gomperts, R. E. Stratmann, O. Yazyev, A. J. Austin, R. Cammi, C. Pomelli, J. W. Ochterski, R. L. Martin, K. Morokuma, V. G. Zakrzewski, G. A. Voth, P. Salvador, J. J. Dannenberg, S. Dapprich, A. D. Daniels, Ö. Farkas, J. B. Foresman, J. V. Ortiz, J. Cioslowski and D. J. Fox, *Gaussian 09*, Wallingford, CT, Gaussian, 2009.
38 S. Grimme, J. Antony, S. Ehrlich and H. Krieg, *J. Chem. Phys.*, 2010, **132**, 154104.
39 F. Allouche, W. Selmi, M. Zid and T. Benlecheb, *J. Mol. Struct.*, 2019, **1179**, 756–763.
40 D. Wu, W. Mi, M. Ji, C. Hao and J. Qiu, *Spectrochim. Acta, Part A*, 2012, **97**, 589–593.
41 Y. Xu, M. Li, Y. Fu, T. Lu, Y. Hu and W. Lu, *J. Mol. Graphics Modell.*, 2019, **86**, 170–178.
42 NIST Computational Chemistry Comparison and Benchmark Database, NIST Standard Reference Database Number 101, Release 15b, August 2011, Editor Russell D. Johnson III, http://cccbdb.nist.gov/.
43 G. T. Velde, F. M. Bickelhaupt, E. J. Baerends, C. F. Guerra, S. J. A. V. Gisbergen, J. G. Snijders and T. Ziegler, *J. Comput. Chem.*, 2001, **22**, 931–967.
44 Q. Peng, Y. Yi, Z. Shuai and J. Shao, *J. Am. Chem. Soc.*, 2007, **129**, 9333–9339.
45 Y. Niu, Q. Peng, C. Deng, X. Gao and Z. Shuai, *J. Phys. Chem. A*, 2010, **114**, 7817–7831.
46 M. Kasha, *Discuss. Faraday Soc.*, 1950, **9**, 14–19.
47 G. Zhao and K. Han, *J. Phys. Chem. A*, 2007, **111**, 9218–9223.
48 G. Zhao, B. H. Northrop, K. Han and P. J. Stang, *J. Phys. Chem. A*, 2010, **114**, 9007–9113.
49 G. Zhao and K. Han, *J. Chem. Phys.*, 2007, **127**, 024306.
50 R. Englman and J. Jortner, *Mol. Phys.*, 1970, **18**, 145–164.
51 Z. Shuai and Q. Peng, *Phys. Rep.*, 2014, **537**, 123–156.